7218 J. Phys. Chem. A 2009, 113, 7218–7226

Modeling Reactive Scattering of F(^{2}P) at a Liquid Squalane Interface: A Hybrid QM/MM Molecular Dynamics Study[†]

Brian K. Radak, Scott Yockel, Dongwook Kim,[‡] and George C. Schatz*

Department of Chemistry, Northwestern University, 2145 Sheridan Road, Evanston, Illinois 60208-3113

Received: October 28, 2008; Revised Manuscript Received: February 20, 2009

To better understand the reactivity of gases with liquid surfaces, experimentalists have recently probed the reactive scattering of atomic fluorine at the surface of liquid squalane ($C_{30}H_{62}$). In this paper we further this research by simulating this scattering process at collision energies of 0.5 and 1.0 eV using a hybrid QM/MM molecular dynamics scheme. To model the structure of the liquid surface, classical molecular dynamics calculations were performed utilizing the OPLS-AA force field. During the F + squalane molecular dynamics simulation, QM/MM calculations are performed at every trajectory step by combining the MSINDO semiempirical Hamiltonian with OPLS-AA and using a dynamic partitioning of the atoms in the QM or MM regions via a “seed atom” method. This computational model provides a type of “on-the-fly” direct dynamics applicable to larger scale chemical processes that include the making/breaking of chemical bonds not available in standard force field models. Our results show that H abstraction is the only reactive scattering pathway and that most trajectories result in reactive scattering. Reaction statistics at the squalane surface are discussed, including variation of the results with incident angle and collision energy, and the probability of reaction as a function of carbon atom type, collision depth, and residence time. Product states, including angular distributions and final translational and rovibrational energies, are also considered and found to be significantly affected by the exothermic reaction energy for H abstraction. The vibrational distributions are in good agreement with recent experiments, but the rotational distributions are dominated by a nonthermal component while the experiments, which involve thermal incident energies, show comparable thermal and nonthermal contributions. Results for O + squalane at 1.0 eV, which we also present, show analogous comparisons with experiment, with OH vibrational distributions which are cold and match experiment, while the calculated rotational distributions are dominated by nonthermal behavior.

I. Introduction

The dynamics of chemical reactions at gas/liquid interfaces are becoming increasingly important in modern chemistry. These reactions are found in biological systems (e.g., the transfer of oxygen and uptake of pharmaceutical agents in blood) as well as in many industrial settings such as the manufacturing of surfactants and heterogeneous catalytic processes. Recently there has also been interest in these reactions as models of the behavior of polymers on the surface of spacecraft in low-Earth orbit. However, despite the many practical applications of interfacial chemistry, a predictive theory of chemical dynamics at interfaces remains elusive. This is not for a lack of research; indeed there is an extensive history of surface chemistry at gas−solid and gas−liquid interfaces over the last few decades, with significant successes in the former. Rather, gas/surface reactions, particularly on liquids, present an entirely different challenge than do bulk phase reactions. Experimentalists and theorists continue to investigate the most simple of systems, using components whose bulk properties are well-known and are amenable to laboratory measurements.

The earliest reported experiments with liquid surfaces were the molecular-beam scattering studies of Hurlbut and Beck.[1] Since then, scattering experiments have remained the dominant method for studying gas−liquid interfacial systems.[2] The two most notable analyses consist of molecular beam studies using time-of-flight analysis and gas jet experiments using a laser to probe the rovibronic states of the nascent products. Both Minton et al.[3] and McKendrick et al.[4] have used these respective techniques to extensively study oxygen collisions with squalane ($C_{30}H_{62}$), a saturated liquid hydrocarbon. Because of its low vapor pressure squalane is an ideal substrate for these experiments. Molecular beam studies have also been conducted with noble gases and squalane[5] and chlorine and squalane.[6]

From these experiments, it has been established that two distinct collision pathways exist and are characterized by the residence time and extent of energy exchange at the liquid surface. Gas molecules residing on the surface for long periods of time undergo significant energy exchange with the surface before scattering and are usually classified as the trapping desorption (TD) component. Conversely, molecules that strike and then quickly leave the surface largely unchanged are often described as the impulsively scattered (IS) component. The latter of these terms may introduce some ambiguity in the present work as it was originally developed to describe entirely nonreactive processes. As such, we will follow the updated nomenclature of Nesbitt et al. and instead refer to this component as the hyperthermal desorption/scattering (HDS) component. The TD reaction channel may occur on a time scale long enough to give rise to an equilibrium distribution of states in accordance with the surface temperature. The shorter time scale of the HDS component can, in turn, give rise to a nonequilibrium inversion

---

[†] Part of the “Robert Benny Gerber Festschrift”.

* To whom correspondence should be addressed. E-mail: schatz@chem.northwestern.edu.

[‡] Present address: School of Chemistry and Biochemistry, Georgia Institute of Technology, Atlanta, GA 30332-0400.

10.1021/jp809546r CCC: $40.75

of rovibronic states. The trajectory conditions (most notably the translational energy, angle of incidence) can be adjusted to influence the branching ratio between these two components.

Nesbitt and co-workers have previously studied the rovibronic states of HF in gas phase experiments via both reactive scattering of F from H_2,[7] methane,[8] and ethane[9] as well as inelastic scattering of HF from various noble gases.[10] Using high-resolution infrared laser absorption methods they are able to obtain quantum state-resolved rovibrational distributions of the nascent HF products. These same techniques were recently extended to reactive scattering of atomic fluorine from squalane by using low incident collision energies ($E_{\mathrm{inc}} \approx 0.7$ kcal/mol = 0.03 eV) to examine the effects of exothermic energy release at the gas–liquid interface.[11] In accordance with the TD and HDS components, they observed a distinctly two-temperature Boltzmann distribution of rotational states, corresponding to TD (305 and 338 K) and HDS (2400 and 1600 K) dynamics for $\nu = 1$ and 2, respectively. In addition, they have calculated the branching ratio ($\alpha_{\mathrm{TD}} = f_{\mathrm{TD}}/(f_{\mathrm{TD}} + f_{\mathrm{IS}})$) between these components to be 0.78 and 0.69 for $\nu = 1$ and 2.

Because of the extensive measurements on O + squalane, there have been several attempts at performing molecular dynamics studies of this system or the related O + alkane-thiol self-assembled monolayer system.[12a] However, the only complete study of O + squalane that included bond breaking was recently performed by our group, using a more advanced QM/MM dynamics method at hyperthermal (5.0 eV) energies.[13] In this paper we present a complementary study of the F(^{2}P) + squalane system, this time considering lower incident energy ($E_{\mathrm{inc}} = 0.5$ and 1.0 eV), with the goal of providing insight concerning this chemically quite distinct system compared to the previously studied O(^{3}P) + squalane reaction. Detailed comparisons with the Nesbitt experiments will be provided, although we note that computational limitations do not allow us to consider collision energies as low as in their measurements. We also present new results for O + squalane at 1.0 eV for comparisons with the F + squalane calculations, and with the McKendrick experiments.

II. Computational Methods

A. Structure of Liquid Squalane. As outlined in a previous work, properly determining the surface structure of liquid squalane is a necessary step to simulating interfacial interactions.[13] Kim et al. have shown that the all-atom OPLS-AA[14] force field more accurately reproduces the experimentally observed bulk density of squalane than MM3. As a result, the OPLS-AA model is used for all simulations. Previous theoretical studies of the structure of liquid squalane, [4c,15] by contrast, used united-atom empirical models.

By using the TINKER 4.1 software package[16] with an isobaric–isothermal (NPT) ensemble, a model liquid containing 48 squalane molecules was generated within a cell under periodic boundary conditions (PBCs). An initial equilibration of the bulk was run for 1.5 ns at 500 K followed by an additional 1.0 ns at 298 K. At this point, the bulk density for squalane was within 2–3% of the experimental value (0.815 g/cm^3). To simulate a liquid slab, the box size (38.5 × 38.5 × 31.5 Å^3) of the last structure of this simulation was extended to add empty space in both directions along the shorter axis (38.5 × 38.5 × 94.5 Å^3). This process, which effectively bypasses the PBCs along the axis, is based upon the previous NVT calculations of Kim et al.[13] Additional canonical ensemble (NVT) simulations were then run for 1.0 ns at 500 K and 1.0 ns at 400 K. Surface structures were then generated by simulation for 2.0 ns at 298 K for final equilibration and data collection. It is this surface that is then used in the F + squalane collision simulations.

B. Dynamics Calculations. Previously, our group has developed a simulation model that merges classical molecular dynamics for the entire system with a quantum mechanical treatment of the atoms in a reaction region(s) at each time step for a type of hybrid QM/MM direct dynamics.[13] This approach combines the computational efficiency of classical molecular mechanics potentials with the superior accuracy of quantum mechanics, and unlike standard molecular mechanics implementations, quantum mechanics also allows for the possibility of bond making/breaking events. The quantum mechanics component is calculated by using the modified symmetrically orthogonalized intermediate neglect of differential overlap (MSINDO) semiempirical Hamiltonian[17] and the molecular mechanics component is implemented by using the OPLS-AA force field as was used in the squalane structural calculations mentioned previously.

A dynamic partitioning of the QM region is used based upon a seed atom algorithm (briefly described here; a more in depth description was published previously[13]). Each atom type is given a characteristic QM radius and all atoms within the QM radius of a seed atom (usually an open shell species) are included in the quantum calculations. The QM radius is defined as the distance between the seed atom and methane at which the force drops below 1.0×10^{-7} hartree/bohr. Using this criterion we find the QM radii to be 10.0, 12.0, and 12.5 bohr for F, H, and C, respectively. Initially, the F atom is the only seed atom, which is also the only open shell atom. As it approaches the surface and additional atoms enter the QM region, bond breaking events may occur. Any new open shell species formed (such as the carbon of a methyl radical) also become a seed atom, and the F atom remains a seed atom throughout the simulation, so that HF is always computed with QM as it leaves the surface. Throughout most of the simulation it is common to have between 75 and 150 atoms being computed in the QM region at each time step, which makes the efficiency of a semiempirical QM method tractable.

In previous QM/MM simulations, the use of MSINDO was justified by its success in describing gas phase reactions involving oxygen and short chain hydrocarbons.[18,19] In Table 1, we make a comparison of the reaction barriers and energies computed with several standard semiempirical (AM1, PM3, MSINDO) methods as well as an advanced ab initio (CCSD(T)) calculation for the F + methane and ethane reactions. These reactions help establish the accuracy of the energetics computed with standard semiempirical methods for hydrogen abstraction from primary carbons. The table shows that overestimation of the exothermic H abstraction reaction energy found with MSINDO is much less than that with the other semiempirical values, 0.142 eV for methane and 0.358 eV for ethane using the ZPE corrected values. It should be noted that there is a significant increase in the overestimation of the exothermicity of the reaction when increasing hydrocarbon size from CH_4 to C_2H_6. However, when comparing the computed hydrogen abstraction barrier heights to the experimental barriers, the overestimation found with MSINDO is less than 0.1 eV for both CH_4 and C_2H_6. Furthermore for comparison, ab initio MP2 computations at the complete basis set limit for F + C_2H_6 reaction barriers were determined to be 0.013 eV by Roberto-Neto and Machado,[20] which is in accord with our MSINDO barrier.

A more detailed analysis of the reaction barriers and enthalpy of fluorine with small hydrocarbons, also including C_3H_8, and

TABLE 1: Reaction Energies (ΔE) and Barriers (Δ$E^‡$) in eV for H Abstraction and H Elimination of F + Methane and Ethane[g]

		AM1	PM3	MSINDO	CCSD(T)[a]	exptl
$CH_4 + F \rightarrow CH_3 + HF$	ΔE	−2.304 (−2.406)	−1.685 (−1.850)	−1.418 (−1.584)	−1.211 (−1.366)	−1.442[b]
	Δ$E^‡$	0.478 (0.167)	0.028 (−0.132)	0.167 (0.112)	0.030 (0.005)	0.019,[c] 0.035[d]
$CH_4 + F \rightarrow CH_3F + H$	ΔE	−0.825 (−0.966)	−0.329 (−0.522)	−0.015 (−0.189)	−0.068 (−0.215)	−0.222[b]
	Δ$E^‡$	1.321 (1.270)	1.249 (1.165)	1.769 (1.660)	1.222 (1.086)	
$C_2H_6 + F \rightarrow C_2H_5 + HF$	ΔE	−2.612 (−2.732)	−2.119 (−2.272)	−1.856 (−2.000)	−1.438 (−1.594)	−1.642,[e] −1.763[f]
	Δ$E^‡$	0.287 (0.131)	−0.184 (−0.353)	0.082 (0.033)		0.016,[c] 0.030[d]

[a] For reaction involving CH_4, values correspond to CCSD(T)/aug-cc-pVTZ from our work and for C_2H_6 values correspond to CCSD(T)/CBS(T-Q) from ref 20. [b] Reaction enthalpies at 0 K from ref 27. [c] Reaction barrier from ref 28. [d] Reaction barrier from ref 29. [e] Reaction enthalpies at 0 K from ref 30. [f] Reaction enthalpies at 0 K from ref 31. [g] Values in parentheses include zero point energy.

i-C_4H_{10}, have very recently been discussed by Layfield et al.[21] In their study, it is shown that the accuracy of standard MSINDO depreciates further for hydrogen abstraction at secondary and tertiary carbon sites; therefore they developed a specific reaction parameter reparametrization (SRP) of MSINDO from CCSD(T) global potential energy surfaces. In the final part of their study, Layfield and co-workers perform direct dynamics collision studies of F + CH_4 and C_2H_6 with their new SRP-MSINDO and the standard MSINDO potentials. Upon hydrogen abstraction, the HF product vibrational distributions in comparison to the experimental values for CH_4 were improved by using SRP-MSINDO; however, for C_2H_6 MSINDO more closely matched the experimental data.

For the CH_3F + H product in Table 1, which is thought to be comparable to an H elimination reaction mechanism in squalane, all of the reaction barriers computed are well above 1.0 eV; so even though the MSINDO barrier is too high, this reaction is not expected to contribute significantly at the energies of interest here. Therefore, we have chosen the use of MSINDO for our F + squalane studies as this provides reasonable energetics (in comparison to other standard semiempirical methods) for the H abstraction mechanism while H elimination should be unimportant at our collision energies.

We chose fluorine translational energies of 0.5 and 1.0 eV in order to achieve low enough incident energy collisions to avoid H elimination yet remain well above the H abstraction barrier. These energies are low enough to enable some connection with the Nesbitt experiments,[11] but at the same time they are high enough to make the time scale of the collisions short enough so that a statistically meaningful number of trajectories could be computed. However, as will be seen, the higher incident energies compared to experiment are such that trapping desorption is not expected to play as important a role. Note that these energies are significantly lower than were considered in the earlier O + squalane study,[13] in which the atomic oxygen had a 5.0 eV incident translational energy.

For each trajectory, the molecular dynamics is restricted to considering a cylindrical “pillbox” (pictured in Figure 1) from the original squalane slab structure. This system has a radius of 20 Å and a depth of 20 Å with respect to the squalane surface (see Results and Discussion). A second cylinder is then nested within this, having a radius and depth of 15 Å. To prevent collapse within the cell during simulation, thus altering the surface density, all atoms in the outer region are given fixed coordinates for the duration of the trajectory; the inner atoms are allowed to move freely (Figure 1).

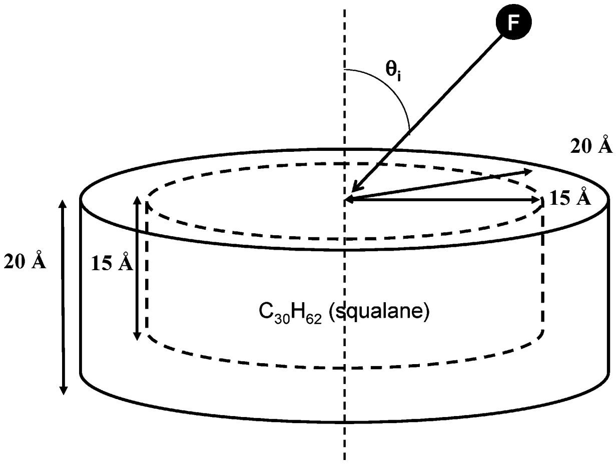

Figure 1. Schematic picture of the simulation region. The outer region is composed of fixed coordinate atoms while atoms in the inner region are allowed to move freely. The trajectory of the incident fluorine atom with an angle of incidence θ_i, is indicated by a single arrow.

In the simulations, the incident fluorine atom is started at 15 bohr above the Gibbs surface (see Results and Discussion) with an initial translational energy of 0.5 or 1.0 eV, any of four azimuthal angles ($\varphi = 0°, 90°, 180°$, or $270°$), and one of three incident angles with respect to the surface normal ($\theta_i = 30°$, $45°$, or $60°$). These initial geometric configurations are the same as were used for the previous O(^{3}P) + squalane simulations and thus are chosen to allow direct comparison. It must be noted that the experimental setup that we compare to later has an F atom source that is normal to the surface with only a very small range of incident angles. At the start of our simulation, the nearest squalane carbon is never closer than 5 bohr from fluorine along the surface normal, and even this situation is highly unlikely (see Results and Discussion). At both energies, all combinations of these angles are run, and in addition, nine different points on each squalane surface are targeted, which results in $4 \times 3 \times 9 = 108$ different trajectories. This is repeated by using 10 different snapshots from the liquid slab simulations to form the initial structure for the surface scattering model. Thus there are a total of 1080 trajectories for each incident translational energy.

All trajectories are set for a total run time of 3.75 ps, unless an atom (almost always a reaction product or inelastically scattered fluorine) reaches 20 bohr above the surface (outside the QM and van der Waals radii of any surface atoms) at which point the simulation is automatically ended. Some unphysical events occasionally occur, namely penetration of the complete slab by fluorine or penetration of the wall between the fixed and moveable regions. These happenings are unavoidable in order to maintain a reasonable level of computational demand. Fortunately this leads to less than 5% of the total trajectories being discarded from the final analysis. Another issue is that truncation of the trajectories at 3.75 ps leads to some HF’s (fortunately a small fraction as we discuss later) which have

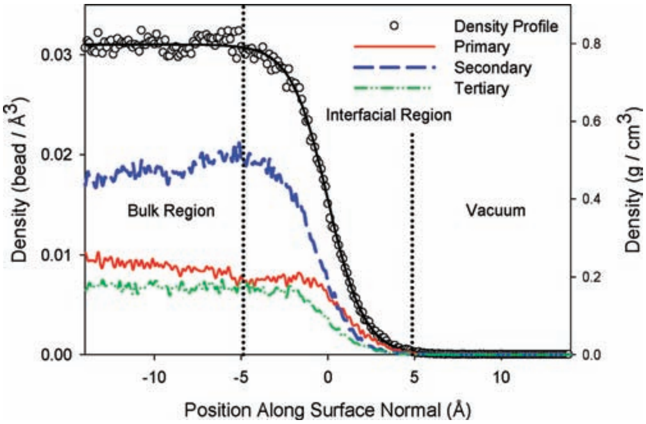

Figure 2. Density profile of the squalane surface (right axis). Boltzmann fitting allows us to obtain the bulk density, position of the Gibbs surface, and width of the interfacial region. Bead density profiles (left axis) for primary, secondary, and tertiary carbons show that the bulk statistics are reproduced except near the surface. Although squalane has twice as many secondary as primary carbons per molecule, at the surface primary carbons compose an excess density.

not escaped from the surface at the end of the collision, but which could subsequently escape, and contribute to thermalized products. These trajectories are included in our analysis, though the data describing the final product state are excluded.

III. Results and Discussion

A. The Squalane Surface. The final NVT simulations at 298 K resulted in 200 squalane structures. The last 191 of these were found to have fully relaxed to equilibrium based on an analysis of the potential energy over time. Since each structure consists of two interfacial regions (above and below), we were able to calculate an average density profile from 382 squalane surfaces as shown in Figure 2. The location of the gas−liquid interface is then taken as the Gibbs dividing surface, that is, the point along the z-axis where the density is half the bulk density. By fitting the density profile to a Boltzmann curve

$$\rho(z) = \frac{\rho_{\mathrm{bulk}}}{1 + \mathrm{e}^{-(z-z_{\mathrm{G}})/b}} \qquad (1)$$

we can obtain the bulk density, ρ_{bulk}, and the position of the Gibbs surface, z_{G}. The parameter b can be thought of as a nominal measure of the width of the interfacial region; this is found to be ∼10 Å. The bulk density is found to be 0.798 g/cm^3 (exptl 0.815 g/cm^3) and all atomic coordinates are shifted such that the Gibbs surface is at 0 Å with respect to the z-axis.

We also calculate the bead densities of primary, secondary, and tertiary carbons, that is, the number density of carbon atoms along the surface normal (Figure 2). In squalane the natural carbon abundances of primary:secondary:tertiary are 8:16:6 and this ratio is clearly reproduced in the bulk beneath the squalane surface. However, above the interface there is an excess of primary carbon density. As was observed in previous simulations of squalane, the C−CH$_3$ bonds of primary carbons are frequently found to be oriented parallel to the surface normal.[12,13] This is again expected to play a significant role in the reaction statistics when fluorine encounters the squalane surface.

B. Reaction Statistics at the Surface. We begin our analysis by addressing the probability of the possible scattering pathways as a function of the incident angle. Reactive scattering is found to dominate at all incident angles and the reactive pathway is limited entirely to H abstraction; H elimination, C−C bond scission, etc. are not observed in any of our trajectories. As explained in Section II, the reaction barrier for H elimination is thought to be larger than 1.0 eV (as it is for methane) and therefore a higher incident translational energy would be needed to see this pathway. Although our trajectories are dominated by H abstraction, there is also significant probability of inelastic scattering (0.22 at 1.0 eV and 0.38 at 0.5 eV) of the F atom as shown in Table 2. This nonreactive pathway becomes more significant at lower energy (0.5 eV) and less direct incident angles (60°) when hard collisions are not as likely to occur. H abstraction occurs almost immediately whenever the fluorine atom encounters hydrogen. Therefore, higher incident energy and more direct angles of incidence lead to more direct collisions and a much higher probability of reaction, rather than inelastic scattering. This effect is most dramatically seen in the statistics for trajectories at 60° incidence; here the decrease in incident energy combined with the “soft landing” causes inelastic scattering to become an equally dominant pathway. Lower incident energies, although more in-line with the experimental conditions, would likely cause the inelastic scattering channel to dominate and thus make it more difficult to gather an adequate number of reactive scattered products for a meaningful statistical analysis. Finally, in general, we found a small fraction of F atom and HF products being trapped after collision, which was 11% at 1.0 eV and 14% at 0.5 eV. One should again note the imposed time limit of 3.75 ps on all trajectories. Even more desorbing trajectories would undoubtedly occur were the simulations continued beyond this point because all trapped gaseous product would eventually desorb, since there is no gaseous pressure above the squalane surface. Considering that there is an increase in the trapped products when going to lower incident energies, it is plausible that if our simulations were at thermal starting energies (i.e., ∼0.05−0.03 eV) there would be a sizable percentage of trapped products at 3.75 ps.

TABLE 2: Reactive Scattering Probability Statistics by Pathway, Initial Fluorine Translational Energy, and Angle of Incidence[a]

		30°	45°	60°	total
1.0 eV	H abstraction	0.84 (0.90)	0.78 (0.95)	0.72 (0.94)	0.78 (0.92)
	inelastic scattering	0.16 (0.91)	0.22 (0.90)	0.28 (0.93)	0.22 (0.86)
0.5 eV	H abstraction	0.71 (0.92)	0.65 (0.86)	0.50 (0.95)	0.62 (0.91)
	inelastic scattering	0.29 (0.94)	0.35 (0.87)	0.50 (0.92)	0.38 (0.83)

[a] Values in parentheses are the probability that the product desorbs from the surface in under 3.75 ps.

Figure 3 depicts the depth of penetration of the fluorine atom, and as would be expected, higher incident energy and more direct impact generally leads to a deeper penetration into the squalane. For our purposes, a collision is defined either as the first reactive event (i.e., the breaking of a bond) or else the first trajectory minimum (i.e., repulsion strong enough to change the F coordinate upward). Analyzing collisions by carbon type, as shown by the bottom graph in Figure 3, offers few surprises if the bead density profiles are taken into consideration; the surface density of primary carbons exceeds that of secondary and tertiary carbons giving rise to an overall more shallow depth of penetration. The large error bars on tertiary carbon reactions, as will be shown later, are due to the low frequency of tertiary carbon collisions; drawing conclusions from these statistics is thus somewhat unreliable.

Table 3 provides additional support for the observed trends in surface penetration, in which we analyze the individual collision probabilities by angle of incidence and carbon type. The first observation to make is that none of the subtotals match

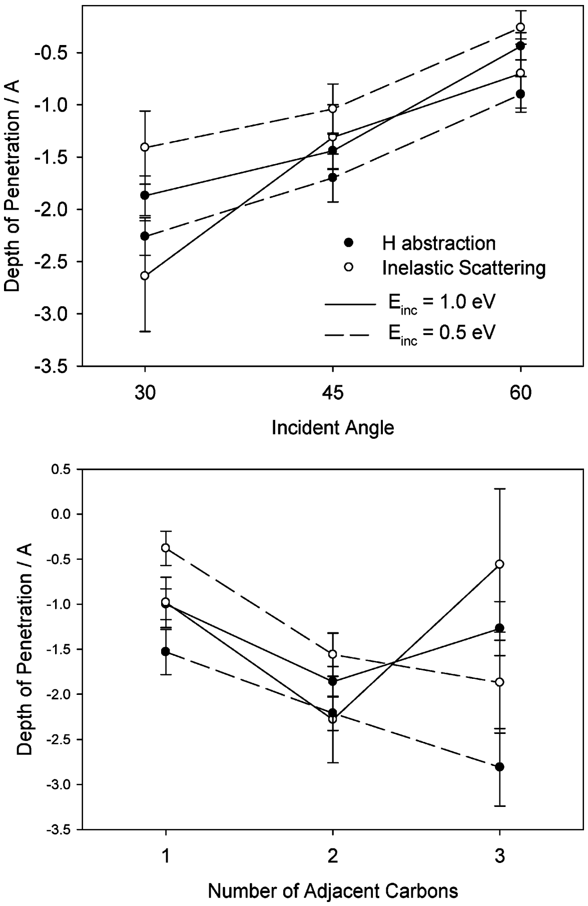

Figure 3. Mean depths of fluorine penetration of the squalane surface for initial translational energy of 1.0 and 0.5 eV versus angle of incidence (top) and carbon type at which scattering/reaction occurred (bottom).

TABLE 3: Reaction Statistics by Carbon Type on Squalane (Primary, Secondary, Tertiary) at Each Incident Angle and Translational Energy (E_T) of Fluorine

E_T		30°	45°	60°	total
1.0 eV	inelastic scattering				
	pri	0.52	0.60	0.57	0.57
	sec	0.41	0.32	0.36	0.36
	ter	0.07	0.08	0.06	0.07
	total	0.24	0.33	0.42	
	H abstraction				
	pri	0.33	0.38	0.42	0.37
	sec	0.51	0.53	0.43	0.49
	ter	0.16	0.10	0.15	0.13
	total	0.37	0.33	0.30	
0.5 eV	inelastic scattering				
	pri	0.57	0.52	0.62	0.58
	sec	0.37	0.45	0.32	0.37
	ter	0.06	0.03	0.06	0.05
	total	0.26	0.31	0.43	
	H abstraction				
	pri	0.25	0.31	0.38	0.28
	sec	0.63	0.57	0.52	0.58
	ter	0.12	0.12	0.20	0.14
	total	0.38	0.35	0.27	

the squalane bulk ratio of carbon type, which is 0.27:0.53:0.20 for primary, secondary, and tertiary carbons, respectively. However, the H abstraction totals are closer to the bulk ratio (0.37:0.49:0.13 at 1.0 eV and 0.28:0.58:0.14 at 0.5 eV), but with more preference for primary over tertiary carbons. It is thought that the lower reaction barrier leads to a preferential reaction with the first hydrogen that is encountered (i.e., a primary carbon). The lack of tertiary carbon chemistry, which is due to shielding, is not likely to change at lower incident energy since adjacent primary carbons will always be present to preferentially react. On the other hand, inelastic scattering occurs most commonly at primary carbons. This also coincides with the trend that less direct incidence angles give rise to more inelastic scattering because a glancing surface collision is most likely to occur near the surface where primary carbons are most common. These trends all appear to hold regardless of the incident energy.

TABLE 4: Mean Residence Times ($\langle\tau_{res}\rangle$, in fs) from Incident Fluorine Atom with Translational Energy (E_T) of 1.0 and 0.5 eV and Incident Angle of 30°, 45°, and 60°[a]

E_T		30°	45°	60°
1.0 eV	inelastic scattering			
	$\langle\tau_{res}\rangle$/fs	872 ± 79	576 ± 59	535 ± 42
	$P(\tau_{res}=0)$	0.30	0.34	0.48
	H abstraction			
	$\langle\tau_{res}\rangle$/fs	686 ± 36	633 ± 35	469 ± 26
	$P(\tau_{res}=0)$	0.31	0.32	0.35
0.5 eV	inelastic scattering			
	$\langle\tau_{res}\rangle$/fs	675 ± 47	633 ± 39	536 ± 28
	$P(\tau_{res}=0)$	0.26	0.36	0.43
	H abstraction			
	$\langle\tau_{res}\rangle$/fs	703 ± 38	647 ± 33	678 ± 36
	$P(\tau_{res}=0)$	0.19	0.37	0.35

[a] $P(\tau_{res}=0)$ represents the probability that the fluorine atom does not cross the Gibbs dividing surface ($x = 0$ in Figure 2).

Lastly, we examine the time scale of residence on the squalane surface, a surface statistic that is inherently linked to the product scattering states. Two variables are measured and the results are listed in Table 4. These are (1) the residence time, τ_{res}, defined as the time between crossings of the Gibbs dividing surface on the incident and return portions of the trajectories and (2) the probability $P(\tau_{res}=0)$ that the residence time is equal to zero, that is, the incident fluorine does not pass through the Gibbs surface. As expected from the mean depth of collision data, deeper penetration from more direct incident angles naturally leads to longer residence beneath the squalane surface. At 0.5 eV, the penetration is more shallow and the probability of desorption from the surface decreases; however, there is no regular shift in the residence times. At 30° incidence, inelastic scattering occurs much faster at 0.5 eV (675 fs) than at 1.0 eV (872 fs); at 60° incidence the residence times are nearly identical. The time scale of H abstraction is largely independent of the incident energy (i.e., the energy released during the reaction is the dominant force). Our findings are in contrast with the much more dramatic trends observed in previous studies involving oxygen at incident energies of 5.0 eV[13] and 1.0 eV.[22] In the studies with oxygen collisions, there is a sizable barrier for H abstraction (~0.5 eV for CH_4)[13] whereas with fluorine, the H abstraction barrier is trivial, as shown in Table 1. In other words, the fluorine has a higher affinity for hydrogen, possibly causing longer residence times when interacting with the squalane surface.

Residence times are perhaps most important because they connect events at the squalane surface with the attributes of the desorbed product via the two limiting cases of trapping-desorption and hyperthermal desorption. It is in this context that we shall proceed to discuss the geometry and energetics of scattering products.

C. Scattering Product Statistics. The recently published infrared studies of Nesbitt and co-workers provide definitive

TABLE 5: HF Vibrational Distribution Ratios $P(\nu{=}2)/P(\nu{=}1)$ by Carbon Type

E_T		pri	sec	ter	total
1.0 eV	$P(\nu{=}2)/P(\nu{=}1)$	0.24 ± 0.058	1.21 ± 0.20	2.94 ± 1.10	0.81 ± 0.098
0.5 eV	$P(\nu{=}2)/P(\nu{=}1)$	0.50 ± 0.12	1.47 ± 0.24	13.67 ± 10.02	1.20 ± 0.14

evidence of vibrationally excited HF products from a liquid squalane surface,[11] with significant population of $\nu = 1$ and 2, which in contrast to HF from gas phase ethane studies is vibrationally more relaxed.[23] Furthermore, their study clearly shows two-temperature Boltzmann behavior in the rotational distributions, due to mechanisms that they refer to as trapping desorption (TD) and hyperthermal desorption/scattering (HDS) dynamics. The former accounts for products thermally accommodated with the surface (305 and 338 K for $\nu = 1$ and 2, respectively) while the latter indicates a rotationally hot component arising from direct scattering after H abstraction (2400 and 1600 K).

In this study, we find the overall vibrational distribution of HF to be distinctly hot. To quantify this, we compute the ratio $P(\nu{=}2)/P(\nu{=}1)$, as shown in Table 5. Previous experimental and theoretical studies of O + squalane[6a,13] have shown these values to differ depending on the type of carbon from which H abstraction occurs; they have suggested that primary carbons lead to lower vibrational excitation while tertiary carbons lead to higher vibrational excitation due to the difference in C−H bond energy. We observe this similar behavior in our study, as tertiary and, to some extent, secondary carbons lead to more excitation, as much as several times the total average for primary carbons. Qualitatively the vibrational distributions agree well with experiment as depicted in Figure 4, with significant population in $\nu = 1$ and 2. As the initial translational energy is reduced from 1.0 to 0.5 eV, better agreement with experiment is observed, in which the population of $\nu = 2$ dominates. The lower population for $\nu = 0$ in the calculations compared to experiment is the only inconsistent behavior predicted in our model of vibrational distributions. This does not appear to be an artifact of the high incident energies since vibrational excitation only seems to increase in going from 1.0 to 0.5 eV. However, a key issue, which we discuss later, is that the experiments have a significant fraction of HF's which have been accommodated with the surface, while the calculations show very little thermal HF. Due to the fact that the experimental incident angle is mostly normal to the surface ($\theta_i = 0$), we provide the uncombined incident angle vibrational data in Figure S1 of the Supporting Information.[24] We find that the trends in vibrational population occur regardless of the incident angle, implying that they can be attributed almost entirely to the energy of the H abstraction reaction and not the energy or geometry of the collision.

Figure 5 presents rotational distributions for the product HF. Nearly all of these distributions are decidedly nonthermal in shape, which is in contrast to what is found in the experiments of Nesbitt and co-workers[11] where both thermal and nonthermal components are found. As stated above, our calculated rotational distributions are expected to be hot compared with experiment because our incident energy is significantly higher, the trajectories are truncated at 3.75 ps, and MSINDO slightly overestimates the reaction energy. In a gas phase scattering study Espinosa-Garcia et al.[25] have also noted that the topology of the potential energy surface along the reaction coordinate can have a profound effect on the rotational distribution of HF. In addition, bimodal distribution in the rotational states of HF from gas phase collision studies has been seen within ab initio dynamics studies by Castillo et al.[26] For the F + squalane reaction, the published spectrum for $\nu = 1$ and 2 shows a thermal component that is clearly missing in our results, and the nonthermal component of the experimental distribution has a colder maximum by ~4 *J*-states, both of which are consistent with our expectations. Our results also show that lower vibrational states are accompanied by increased rotational excitation, which is a typical result for gas phase chemistry that is also seen in the experiments. However, the shapes of the $\nu = 0$, 1 distributions are in general quite similar, as are the $\nu = 2$, 3 distributions (see Figure S2 in the Supporting Information).[24]

Past experimental data[3,11] have already suggested that some rotational relaxation of the nascent product occurs before desorption and detection, whereas vibrational relaxation occurs on a longer time scale. To study this, we have analyzed the trajectories according to residence times, as is shown in Figure 6, in order to understand the mechanisms by which HF become thermally equilibrated with the surface. In Figure 6, the rotational distributions are split into three groups of residence

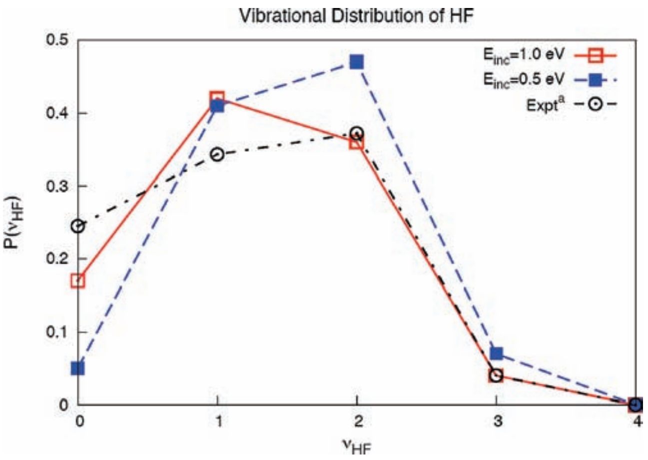

Figure 4. Distribution of vibrational states of HF leaving the squalane surface including 1.0 and 0.5 eV input translational energy.

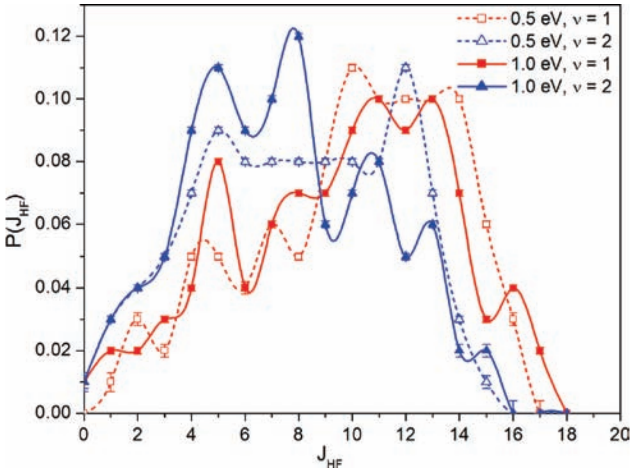

Figure 5. Distribution of rotational states in $\nu = 1$ (red) and $\nu = 2$ (blue) vibrational states of HF leaving the squalane surface. Solid lines are from 1.0 eV and dashed lines are from 0.5 eV input translational energy.

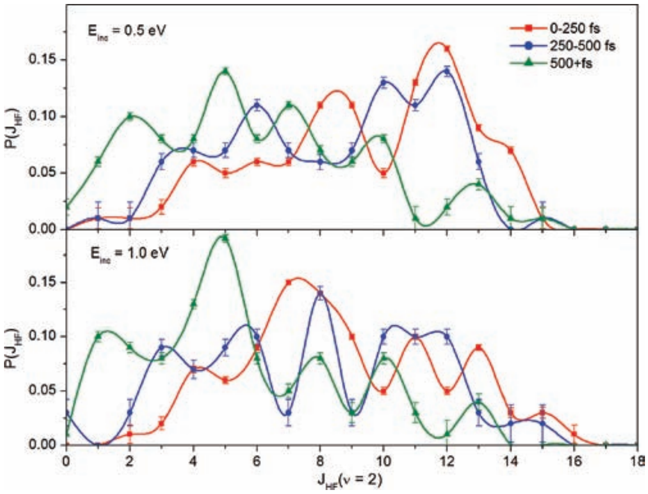

Figure 6. Rotational states from $\nu = 2$ of desorbed HF grouped by resident time for both 0.5 (top) and 1.0 eV (bottom) incident translational energies.

times (0−250, 250−500, 500+ fs), which were chosen based on groupings found in scatter plots of residence times and rotational states (see Figure S3 in the Supporting Information).[24] Interestingly, the trajectories with residence times greater than 500 fs are clearly more rotationally relaxed and more Boltzmann-like than those reactions that occur much faster. The "middle" component shares characteristics of both. Knowing that at lower incident energies more products would be trapped after 3.75 ps and that longer residence times lead to rotational relaxation, it is plausible that these trapped products would contribute significantly to a thermal component in the rotational distribution. This distinction matches the conclusions of Nesbitt and co-workers, and helps to shed light on what length of resident times are needed for complete thermal equilibration with the surface.

To provide further insight into the rotational and vibrational distributions, we have calculated O + squalane trajectories at 1.0 eV that are comparable to those of our earlier study at 5.0 eV.[13] As expected, we find that the OH vibrational distribution is dominated by $\nu = 0$, with the ratio of $\nu = 1/\nu = 0$ populations being 0.05 ± 0.02 in these calculations. This ratio is only slightly below our earlier 5.0 eV result of 0.13, and it compares well with the McKendrick measurements[4b] of 0.07 ± 0.02 for incident energies of 0.16 eV. This suggests that vibrational excitation is largely determined by energy release during the reaction (meaning that reagent translational energy does not play a major role), and that vibrational relaxation as the OH exits from the squalane is small. Both conclusions are analogous to what we find for F + squalane.

The OH rotational distribution for 1.0 eV collision energy is plotted in Figure 7. Only the sum over vibrational states is plotted, as there are too few trajectories for $\nu = 1$ to generate a statistically significant result. We see that this distribution, which is dominated by OH(ν=0), is actually somewhat comparable to the $\nu = 1$ distribution for HF at 1.0 eV in Figure 5, with a substantial nonthermal component. This comparison is only of qualitative significance as the energy release and rotational dynamics of these two reactions are only roughly similar; however, what it does show is that the dynamics in both cases is dominated by nonthermal behavior. Of more direct relevance is the comparison of the OH(ν=0) rotational distribution from the McKendrick experiments,[4b] where the thermal component of the distribution was dominant. This indicates a somewhat comparable situation to what we have found for F + squalane, where the experiment shows a much more significant thermal component than we have calculated. It is also noteworthy that the rotational distribution calculated earlier for O + squalane at 5.0 eV shows a maximum at $J_{OH} \approx 5$, which is lower than the $J_{OH} \approx 12$ maximum at 1.0 eV. The low rotational excitation component at higher energies was previously attributed to an important trapping/desorption component. At 1.0 eV there is less penetration into the squalane, and therefore less trapping, so the rotational distribution has a less significant low J_{OH} peak. Somewhat comparable behavior is apparent for F + squalane (Figure 5) in the comparison of 0.5 and 1.0 eV results.

The final scattering angle and translational energy of the products for F + squalane are also of particular interest to the scattering processes. However, to our knowledge the relevant molecular beam studies for the F + squalane system have not been conducted. Figures 8 and 9 present the results, and we see that both distributions vary significantly between inelastic and reactive scattering products. In particular the H abstraction products nearly always scatter closer to the surface normal (Figure 8, bottom) than the inelastically scattered fluorine (Figure 8, top). This is especially the case at 0.5 eV (Figure 8,

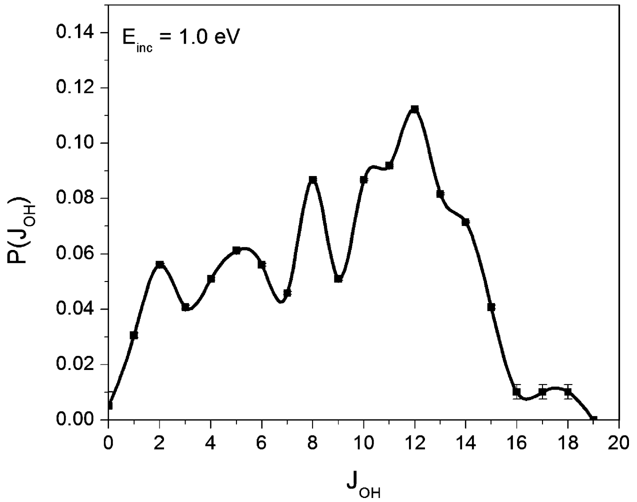

Figure 7. Total distribution of rotational states of OH leaving the squalane surface including all vibrational states (nearly all vibrational states are from $\nu = 0$, $P(\nu_{OH}) = 0.95$).

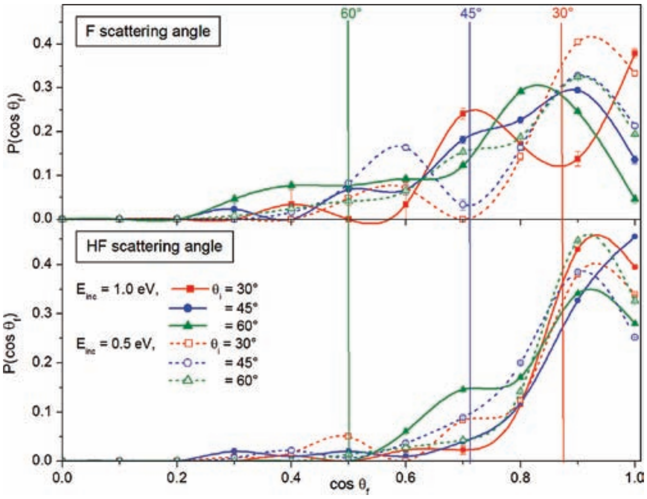

Figure 8. Distribution of the product scattering angle with respect to the surface normal (θ_f) of the scatter F (top) and HF (bottom). Vertical lines represent the purely specular scattering.

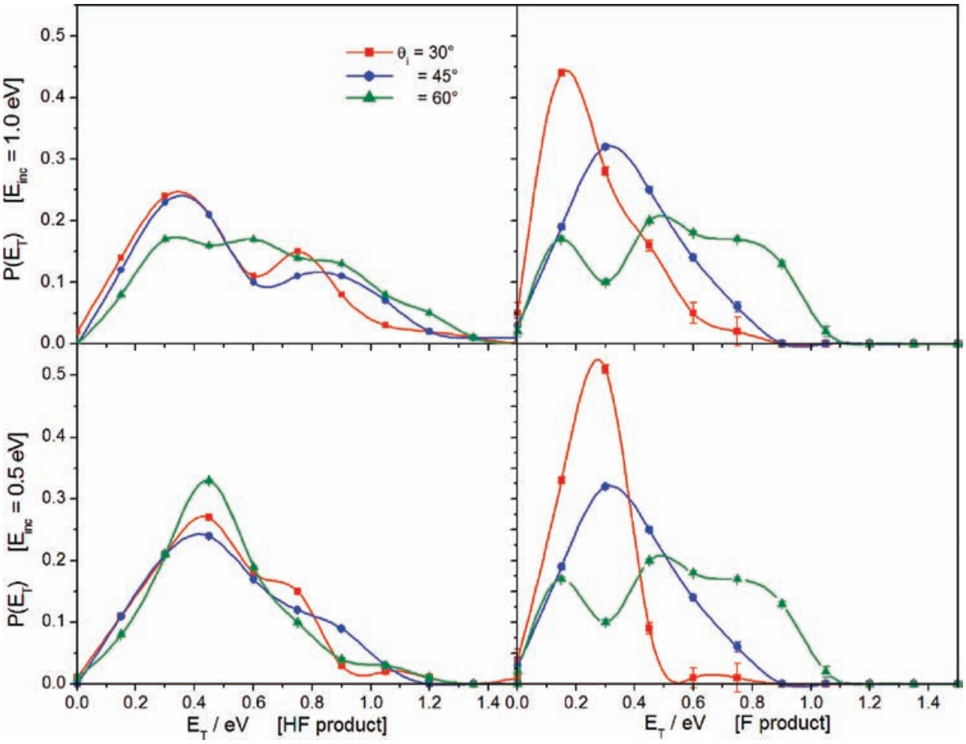

Figure 9. Distribution of product translational energies (in eV) of HF (left) and scattered F (right) from both incident translational energies 1.0 (top) and 0.5 eV (bottom) and for each incident angle 30°, 45°, and 60°.

bottom dashed lines), where almost half of the trajectories scatter with $\theta_f < 30$ °. Inelastic scattering (Figure 8, top) gives rise to much broader distributions, which seem to reflect the effects of surface roughness. The "harder" impacts at 1.0 eV (Figure 8, right solid lines) increase the effects of surface roughness, giving rise to the broadest distributions. The closest behavior to specular scattering comes from the inelastic scattering of fluorine atoms at 30° incident angle and 0.5 eV incident energy.

As shown in Figure 9, HF also gains significant translational energy after reaction, frequently leaving with more than the incident energy. This is most dramatic at 0.5 eV where the HF products have anywhere from 1.5 to 2.0 times as much translational energy as they started with (Figure 9, bottom left). For both reactive and nonreactive processes, the less direct angles of incidence lead to higher product translational energies. However, the effect is visibly diminished at 0.5 eV when there is clearly less energy transfer at the surface. This decrease in energy transfer is most pronounced for inelastic scattering where there is no energy release from reaction.

IV. Conclusion

Here we have presented a study of gas−liquid interface dynamics using hybrid QM/MM dynamics. The squalane liquid used is common to many experiments as well as in a previous theoretical study within our group of O + squalane. However, the use of fluorine as the impinging gas greatly changes the energetics of reaction compared to oxygen because the H abstraction reaction has a low barrier and is highly exothermic. The energy release following reaction causes significantly different dynamics between the inelastic and reactive scattering pathways. Even though we use incident energies significantly higher than in the experiment by Nesbitt et al., the possibility of other reactive pathways such as H elimination and C−C bond scission is still negligible, as these reactions have much larger barriers. We have shown that our computed vibrational distributions agree well with experimentally determined values and that the observed rotational distributions agree qualitatively with the nonthermal component of the measured distribution. We attribute the absence of a thermal component as well as other errors to our increased incident energy, the truncated trajectory integration time, as well as a slight overestimation of reaction enthalpies by the MSINDO Hamiltonian that was used. We also provide insight to the cooling of rotational excitations of products that are seen in the trapping desorption and hyperthermal desorption components by segregating trajectories on the basis of residence time and depth of reaction. Vibration/rotation distributions for O + squalane at 1.0 eV have also been presented, and we find that although the fluorine and oxygen atom reactions have significant differences due to the much larger energy release to the HF product compared to OH, the dynamical processes that arise from the presence of the squalane surface are comparable. We have also presented scattering angle and translational energy distributions as might be obtained from a molecular beam study. Our results show a broad distribution of scattering angle for the inelastic processes, but for the reactive scattering process, the product angular distribution favors the surface normal. Translational energy distributions show that for inelastic scattering the final translational energy is strongly dependent on the incident angle, with more energy being transferred to the liquid via collisions at more direct incident angles and higher incident energy. This trend, however, is not observed for H abstraction where the exothermic energy of reaction overshadows the initial translational energy causing noticeably more energetic scattering products.

Acknowledgment. This research was supported by AFSOR Grant FA9550-07-1-0095. The authors wish to thank David J. Nesbitt (University of Colorado) and Tim Minton (Montana State) for helpful discussions.

Supporting Information Available: Plots of the distribution of vibraional states, the rotational distributions, and rotational states versus residence time of each HF leaving the squalane surface. This material is available free of charge via the Internet at http://pubs.acs.org.

References and Notes

(1) Hurlbut, F. C.; Beck, D. E. U.C. Eng. Proj. Report HE-150-166, University of California, 1959. (For a more complete history and list of pioneering experimentalists, see ref 2 and references therein.)

(2) Nathanson, G. M.; Davidovits, P.; Worsnop, D. R.; Kolb, C. E. *J. Phys. Chem.* **1996**, *100*, 13007.

(3) (a) Zhang, J.; Garton, D. J.; Minton, T. K. *J. Chem. Phys.* **2002**, *117*, 6239. (b) Zhang, J.; Upadhyaya, H. P.; Brunsvold, A. L.; Garton, D. J.; Minton, T. K. *J. Phys. Chem. B* **2006**, *110*, 12500.

(4) (a) Kelso, H.; Köhler, S. P. K.; Henderson, D. A.; McKendrick, K. G. *J. Chem. Phys.* **2003**, *119*, 9985. (b) Köhler, S. P. K.; Allan, M.; Kelso, H.; Henderson, D. A.; McKendrick, K. G. *J. Chem. Phys.* **2005**, *122*, 024712. (c) Köhler, S. P. K.; Allan, M.; Costen, M. L.; McKendrick, K. G. *J. Phys. Chem. B* **2006**, *110*, 2771.

(5) Saecker, M. E.; Nathanson, G. M. *J. Chem. Phys.* **1993**, *99*, 7056.

(6) (a) Garton, D. J.; Minton, T. K.; Alagia, M.; Balucani, N.; Casvecchia, P.; Volpi, G. G. *J. Chem. Phys.* **2000**, *112*, 5975. (b) Garton, D. J.; Minton, T. K.; Alagia, M.; Balucani, N.; Casvecchia, P.; Volpi, G. G. *J. Chem. Phys.* **2001**, *114*, 5958.

(7) Chapman, W. B.; Blackmon, B. W.; Nizkorodov, S.; Nesbitt, D. J. *J. Chem. Phys.* **1998**, *109*, 9306.

(8) Harper, W. W.; Nizkorodov, S. A.; Nesbitt, D. J. *J. Chem. Phys.* **2000**, *113*, 3670.

(9) Whitney, E. S.; Zolot, A. M.; McCoy, A. B.; Francisco, J. S.; Nesbitt, D. J. *J. Chem. Phys.* **2005**, *122*, 124310.

(10) Chapman, W. B.; Weida, M. J.; Nesbitt, D. J. *J. Chem. Phys.* **1997**, *106*, 2248.

(11) (a) Zolot, A. M.; Harper, W. W.; Perkins, B. G.; Dagdigian, P. J.; Nesbitt, D. J. *J. Chem. Phys.* **2006**, *125*, 021101. (b) Zolot, A. M.; Dagdigian, P. J.; Nesbitt, D. J. *J. Phys. Chem.* **2008**, *129*, 194705.

(12) (a) Troya, D.; Schatz, G. C. *J. Chem. Phys.* **2004**, *120*, 7696. (b) Li, G.; Bosio, S. B. M.; Hase, W. L. *J. Mol. Struct.* **2000**, *556*, 43. (c) Köhler, S. P. K.; Allan, M.; Reed, S. K.; Westacott, R. E.; McKendrick, K. G. *J. Phys. Chem. B* **2006**, *110*, 11717.

(13) Kim, D.; Schatz, G. C. *J. Phys. Chem. A* **2007**, *111*, 5019.

(14) Jorgensen, W. L.; Maxwell, D. S.; Tirado-Rives, J. *J. Am. Chem. Soc.* **1996**, *118*, 11225.

(15) Wick, C. D.; Siepmann, J. I.; Schure, M. R. *Anal. Chem.* **2002**, *74*, 3518.

(16) Ponder, W.A.; Richards, F. M. *J. Comput. Chem.* **1987**, *8*, 1016.

(17) (a) Ahlswede, B.; Ju, K. *J. Comput. Chem.* **1999**, *20*, 563. (b) Ahlswede, B.; Ju, K. *J. Comput. Chem.* **1999**, *20*, 572.

(18) Troya, D.; Pascual, R. Z.; Garton, D. J.; Minton, T. K.; Schatz, G. C. *J. Phys. Chem. A* **2003**, *107*, 7161.

(19) Troya, D.; Pascual, R. Z.; Schatz, G. C. *J. Phys. Chem. A* **2003**, *107*, 10497.

(20) Roberto-Neto, O.; Machado, F. B. C. *Chem. Phys. Lett.* **2007**, *449*, 67.

(21) Layfield, J. P.; Sweeney, A.; Troya, D. To be submitted for publication.

(22) Kim, D.; Schatz, G. C. Unpublished results.

(23) Harper, W. W.; Nizkorodov, S. A.; Nesbitt, D. J. *J. Chem. Phys.* **2000**, *113*, 3670.

(24) See the Supporting Information for this article.

(25) Espinosa-Garcia, J.; Bravo, J. L.; Rangel, C. *J. Phys. Chem. A* **2007**, *111*, 2761.

(26) Castillo, J. F.; Aoiz, F. J.; Banares, L.; Martinez-Nunez, E.; Fernandez-Ramos, A.; Vazquez, S. *J. Phys. Chem. A* **2005**, *109*, 8459.

(27) Chase, M. W., Jr. NIST-JANAF Thermochemical Tables. *J. Phys. Chem. Ref. Data* **1998**, *28*, 1.

(28) Persky, A. *Chem. Phys. Lett.* **2003**, *380*, 286.

(29) Maricq, M. M.; Szente, J. J. *J. Phys. Chem.* **1994**, *98*, 2078.

(30) (a) P. Hubert, P.; Herzberg, G. *Molecular Spectra and Molecular Structure Constants of Diatomic Molecules*; Van Nostrand Reinhold: New York, 1979. (b) Baldwin, R.; Drewery, G. R.; Walker, R. W. *J. Chem. Soc., Faraday Trans.* **1984**, *80* (1), 2827.

(31) Gurvich, L. V.; Veyts, I. V.; Alcock, C. B. *Thermodynamic Properties of Individual Substances*, 4th ed.; Hemisphere Pub. Co.: New York, 1989.

JP809546R